Energy 263 (2023) 125897

Contents lists available at ScienceDirect

Energy

journal homepage: www.elsevier.com/locate/energy

Performance simulation and key parameters in-plane distribution analysis of a commercial-size PEMFC

Zhuo Zhang [a,b], Qi-yao Wang [c,d], Fan Bai [a,b], Li Chen [a,b], Wen-quan Tao [a,b,*]

[a] Shaanxi Collaborative Innovation Center for Performance Improvement of PEMFC, Xi'an, 710049, PR China
[b] Key Laboratory of Thermo-Fluid Science & Engineering of MOE, Xi'an Jiaotong University, Xi'an, 710049, PR China
[c] Dongfang Electric (Chengdu) Hydrogen Fuel Cell Technology Co., Ltd., Chengdu, Sichuan, 611731, PR China
[d] Long Life Fuel Cell Key Laboratory of Sichuan Province, Chengdu, Sichuan, 611731, PR China

ARTICLE INFO

Keywords:
PEMFC
Current density
Flow field
Large-scale
Flow direction

ABSTRACT

Commercial fuel cell stacks often have a large electrode area to obtain a high power output. Uniformity in-plane distribution of vital physical quantities plays a key role in improving cell performance and avoiding degradation. In this study, a three-dimensional two-fluid multiphase model is adopted to analyze the in-plane distribution characteristics of key parameters (reactant concentration, temperature, local current density, and membrane water content) for a large-scale PEMFC with an active area larger than 300 cm^2. The particular feature of the PEMFC studied is that there are gap zones near the edge between the bipolar plate and gas diffusion layer and membrane. The results show that for the structure without gap zones, the cell performance improved by about 1%. The non-uniformity of cathode reactant distribution is generally higher than that of the anode; The non-uniformity of temperature in the *x* direction is higher than that in the *y* direction (flow-direction). With the increase of average current density, the temperature in the membrane increases, and the membrane dehydrates gradually. The flow direction of coolant has a significant impact on the cell performance. When coolant is in the same direction as hydrogen, the cell performance decreases by about 3.75% at 0.8 A/cm^2.

1. Introduction

Proton exchange membrane fuel cell (PEMFC) is an energy conversion device that directly converts chemical energy to electrical energy. It has broad application prospects due to its high efficiency, low operating temperature, fast start-up and no-pollution [1,2]. A single PEMFC usually consists of bipolar plate (BP), gas diffusion layer (GDL), microporous layer (MPL), and catalyst layer (CL) in both anode and cathode sides, with the membrane (MEM) sandwiched in the middle. Although the chemical reaction principle of PEMFC is relatively simple, the physical and chemical phenomena involved are very complex. For example, in the catalyst layer, several transport processes and chemical reaction happen simultaneously. In addition to the conduction of electrons and protons, there is also the transport of reactants and products of the chemical reaction. Then, complex heat transfer process follows. Completely and deeply understanding the complex multi-physics, multi-scale transport phenomena in a PEMFC is the key to its performance improvement [3–5].

In the commercial application scenarios, to achieve high output power, PEMFC works in the form of a stack, and the fuel cell stack usually needs hundreds of single cells with a large active area for each cell [6]. For such a large-scale PEMFC, the uneven distributions of reactant, temperature, and current density in the active area (in-plane direction) have more prominent effects than their effects on laboratory-level fuel cell. These non-uniform physical quantities may cause gas starvation, flooding, and catalyst carbon corrosion, and they further cause degradation of PEMFC's performance and lifetime [7]. To investigate various non-uniform distributions of the physical quantities inside a PEMFC, researchers have designed and carried out many in-site measurement techniques [6,8–19].

For example, Chen et al. obtained the water distribution of the gas diffusion layer in a working PEMFC by neutron radiography [8]. Xiao et al. designed a transparent single fuel cell to characterize the water distribution [9]. Chevalier et al. used a synchrotron X-ray radiographic imaging method to measure liquid water content in an operating PEMFC and firstly determine the precision and accuracy of this method [10]. Besides, Suzuki et al. investigated the through-plane water content distribution utilizing magnetic resonance imaging [11]. Based on actual PEMFC, Cheng et al. focused on analyzing the reactants and water

* Corresponding author. Shaanxi Collaborative Innovation Center for Performance Improvement of PEMFC, Xi'an, 710049, PR China.
E-mail address: wqtao@mail.xjtu.edu.cn (W.-q. Tao).

https://doi.org/10.1016/j.energy.2022.125897
Received 27 April 2022; Received in revised form 13 October 2022; Accepted 24 October 2022
Available online 29 October 2022
0360-5442/

Nomenclature

A_p	pore surface area per unit volume(m^2/m^3)
a_w	water activity
c_p	specific heat capacity(J/(kg·K))
D	diffusivity(m^2/s)
r_p	pore diameter(m)
EW	equivalent molecular weight of dry membrane(kg/kmol)
F	Faraday's constant(C/kmol)
j	reaction velocity(A/m^3)
K	permeability(m^2)
l	length
M	molar mass(kg/kmol)
p	pressure(Pa)
p_c	capillary pressure (Pa)
R	gas constant (J/(mol K))
RH	relative humidity
S	source term
s_{lq}	liquid saturation
T	temperature(K)
TP	through-plane
IP	in-plane
$\vec{u}$	velocity(m/s)
w	ionomer volume fraction
x	mole fraction
$\widehat{X}$	certain physical quantity
X	depth(m)
Y	mass fraction
lh	latent heat

Greek letters

ε	porosity
α	transfer coefficient
σ	surface tension coefficient(N/m)
δ	width(m)
θ	contact angle
ρ	density(kg/m^3)
μ	dynamic viscosity (Pa·s)
κ	electrical conductivity (S/m)
γ',γ	phase change rate(1/s)
ξ	stoichiometry ratio
ζ	concentration difference index
η	over potential (V)
φ	potential(V)
φ	auxiliary variable
λ	membrane water content
ΔS	entropy production (J/(kmol·K))

Subscripts and superscripts

a	anode
act	activation
BP	bipolar plate
c	cathode
CL	catalyst layer
EOD	electro-osmotic drag coefficient
eff	effective value
ele	electronic
eq	equilibrium water content
fl	fluid
g	gas
GDL	gas diffusion layer
vp,vap	water vapor
i	certain gas species
ion	proton
Kn	Knudsen diffusion
l,lq	liquid water
lh	latent heat
m	mass
mw	membrane water
m-l	membrane water to liquid (vice verse)
MEM	membrane
MPL	microporous layer
reac	reaction produced water
ref	reference value
sat	saturation
v-l	vapor to liquid
v-m	vapor to membrane water (vice verse)

content distribution and change trends under different humidification conditions [12].

For current density and temperature distribution, Peng et al. adopted the printed circuit board (PCB) approach to measuring the current density distribution of a 20-cell stack with 250 cm^2 active area per cell [6]. Some additional temperature sensors in the PCB were used to measure the temperature distribution of the BP. Yin et al. designed a segmented fuel cell device to measure the one-dimensional current density, humidity, and temperature distribution along a single straight flow channel [13]. Belhadj et al. used a segmented current measurement sensor plate to investigate the current density distribution in a single commercial 100 cm^2 PEM fuel cell [14]. Huang et al. studied the heat pipe application in PEMFC and introduced the temperature uniformity index. In their experiment, grooves were made in a cathode flow field plate to insert thermocouples [15]. Akimoto et al. used a tri-axial magnetic sensor probe to measure current density distribution in the PEMFC stack [16]. Lin et al. investigated the evolution of the temperature and current density distribution at different regions in the constant voltage mode of the stack by the segmented technology [17,18]. The variation of current density distribution in a commercial-size PEM fuel cell under dynamic gas operation parameters was analyzed [18]. Furthermore, a low temperature durability and consistency analysis was performed on a 5-cells stack through different in situ characterization methods [19].

In all these researches mentioned above, some maldistributions of related physical parameters are revealed, which provides important and necessary experimental results for the study in this regard. However, some shortages still exist. High cost and limited resolution are conventional disadvantages of experimental measurements. Besides, a particularly important drawback of most measurement techniques (such as the printed circuit board, segmented fuel cell, etc.) is their invasive feature. It definitely changes the original distributions and inherently reduces the reliability of some measurement results. For example by comparison the tested polarization curve before and after inserting nine microsensor of temperature measurement, Tang et al. found that the two curves deviate about 5% [20].

With the development of computers, numerical simulation has become a feasible and convenient way to obtain the physical quantities distributions in PEMFC. Many studies have shown that the simulation results are in good agreement with the distribution of key physical quantities measured by experiments [21–23]. It has become a powerful tool to obtain the fine distribution results at a low cost..

Falaguerra developed a PEMFC half-cell model (active area 12.5 cm^2) in the cathode and statistically analyzed the current density distribution on the active area of the electrode [24]. Chen et al. studied the impacts of seven critical operating parameters on internal gas

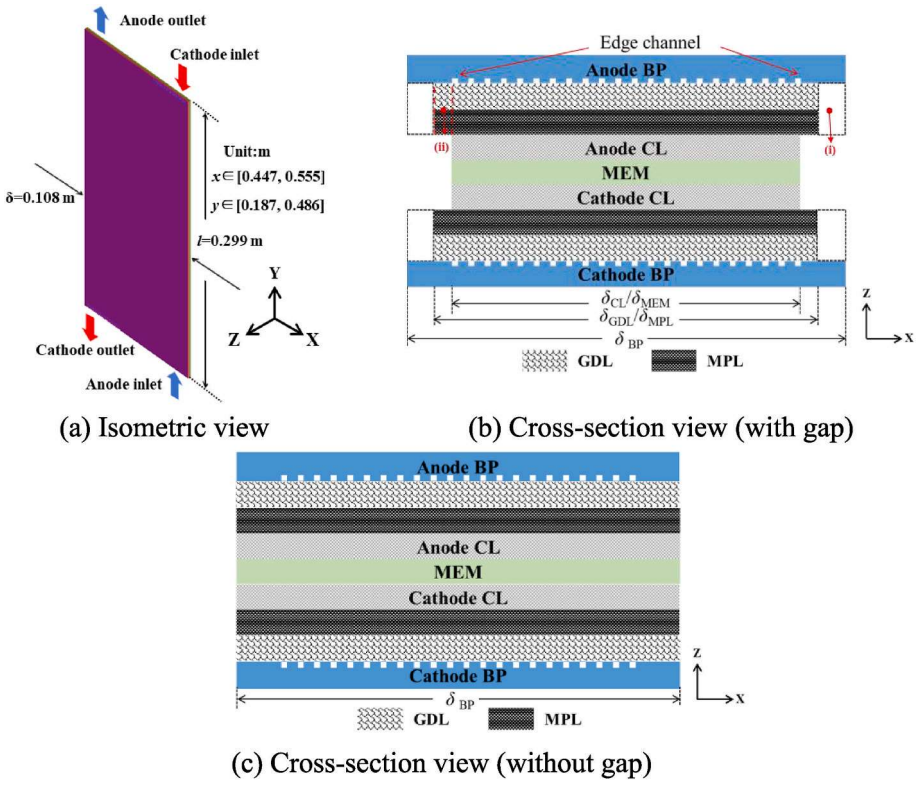

Fig. 1. Computational domain.

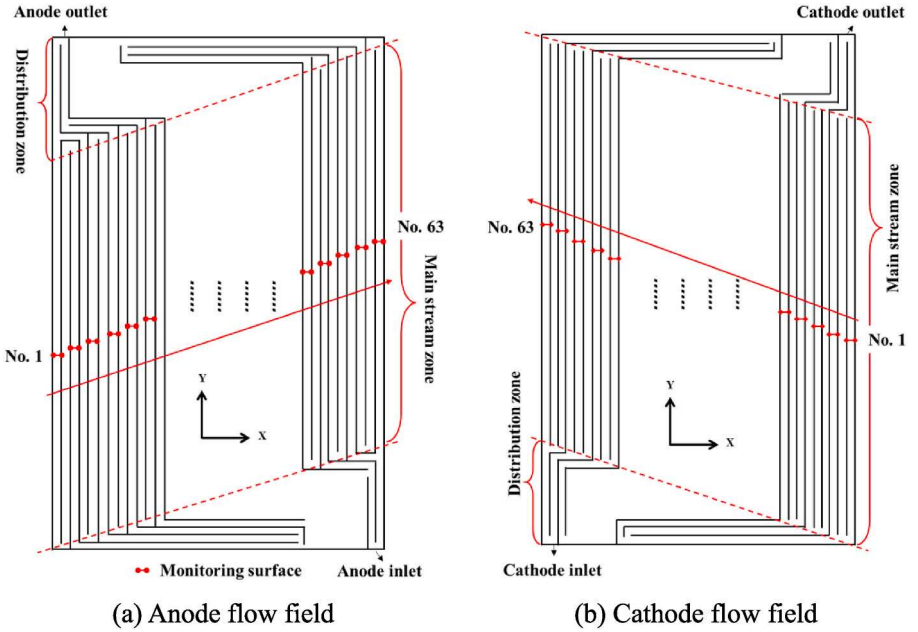

Fig. 2. Flow channel arrangement.

concentration based on a 3-channel serpentine flow field fuel cell (active area 53.3 cm^2). They analyzed the mean value and standard deviation of oxygen distribution [25]. Cheng et al. studied the effect of humidification on the distribution and uniformity of reactants and water content in PEMFC (active area 80 cm^2) [26]. Zhang et al. performed the numerical simulation based on a repeated unit (active area a little over 100 cm^2) in a commercial PEMFC stack [27]. The effects of operating pressure, coolant flow direction on reactant concentration, etc., were studied. It was found that cooling pattern is a key factor affecting temperature distribution and cell performance. Liu et al. pointed out that keeping the cooling water flow direction of the anode and cathode consistent with the cathode gas flow direction is the best pattern [28]. Except for better cooling performance, the optimal cooling patterns also have obvious advantages of PEMFC system integration and cost reduction [28]. Generally, existing literature mostly focuses on the laboratory level (with an active area of no more than 100 cm^2) fuel cell. The computing domain of the above research usually contains only typical units or mainstream zone, while the distribution area in the commercial fuel cell

Table 1
Source terms.

Source terms	Unit
Mass conservation equation: $S_m = S_{H_2} + S_{O_2} + S_{vp}$ (all zones)	kg/(m^3·s)
Momentum conservation equation: $S_u = \begin{cases} -\frac{\mu_g}{K_g}\vec{u}_g & \text{(CLs, GDLs and GDLs)} \\ 0 & \text{(other zones)} \end{cases}$	kg/(m^2·s^2)
H_2 conservation equation: $S_{H_2} = \begin{cases} -\frac{j_a}{2F}M_{H_2} & \text{(anode CL)} \\ 0 & \text{(other zones)} \end{cases}$	kg/(m^3·s)
O_2 conservation equation: $S_{O_2} = \begin{cases} -\frac{j_c}{4F}M_{O_2} & \text{(cathode CL)} \\ 0 & \text{(other zones)} \end{cases}$	kg/(m^3·s)
Water vapor conservation equation: $S_{vp} = \begin{cases} -S_{v-l} + S_{v-m}M_{H_2O} & \text{(anode CL)} \\ -S_{v-l} & \text{(cathode CL, MPLs, GDLs)} \\ 0 & \text{(other zones)} \end{cases}$	kg/(m^3·s)
Condensation/evaporation: $S_{v-l} = \begin{cases} \frac{A_p}{r_p}D^c_{vap}\gamma\epsilon(1-s_{lq})(\rho_{vap}-\rho_{sat}), \rho_{vap} > \rho_{sat} \\ \frac{A_p}{r_p}D^c_{vap}\gamma\epsilon s_{lq}(\rho_{vap}-\rho_{sat}), \rho_{vap} < \rho_{sat} \end{cases}$	kg/(m^3·s)
Electrons conservation equation: $S_{ele} = \begin{cases} -j_a & \text{(anode CL)} \\ j_c & \text{(cathode CL)} \\ 0 & \text{(other zones)} \end{cases}$	A/m^3
Protons conservation equation: $S_{ion} = \begin{cases} j_a & \text{(anode CL)} \\ -j_c & \text{(cathode CL)} \\ 0 & \text{(other zones)} \end{cases}$	A/m^3
Liquid saturation conservation equation: $S_{slq} = \begin{cases} S_{v-l} & \text{(anode CL, MPLs, GDLs)} \\ S_{m-l}M_{H_2O} + S_{v-l} & \text{(cathode CL)} \\ 0 & \text{(other zones)} \end{cases}$	kg/(m^3·s)
Membrane absorption and desorption: $S_{m-l} = S_{m-v} = \frac{\rho_m}{EW}(\lambda_{mw} - \lambda_{eq})\gamma'$	mol/(m^3·s)
Dissolved water conservation equation: $S_{mw} = \begin{cases} -S_{m-v} + S^a_{EOD} & \text{(anode CL)} \\ \frac{S^a_{EOD}V^a_{CL} + S^c_{EOD}V^c_{CL}}{V_{MEM}M_{H_2O}} & \text{(membrane)} \\ -S_{m-l} + S^c_{EOD} + S_{reac} & \text{(cathode CL)} \\ 0 & \text{(other zones)} \end{cases}$	mol/(m^3·s)
Energy conservation equation: $S_E = \begin{cases} j_a\lvert\eta_{act}\rvert + \lVert\nabla\varphi_{ele}\rVert^2\kappa^{eff}_{ele} + \lVert\nabla\varphi_{ion}\rVert^2\kappa^{eff}_{ion} + S_{lh} & \text{(anode CL)} \\ \frac{j_cT\Delta S}{4F} + j_c\lvert\eta_{act}\rvert + \lVert\nabla\varphi_{ele}\rVert^2\kappa^{eff}_{ele} + \lVert\nabla\varphi_{ion}\rVert^2\kappa^{eff}_{ion} + S_{lh} & \text{(cathode CL)} \\ \lVert\nabla\varphi_{ele}\rVert^2\kappa^{eff}_{ele} + S_{lh} & \text{(GDL, MPL)} \\ \lVert\nabla\varphi_{ele}\rVert^2\kappa^{eff}_{ele} & \text{(BP)} \\ \lVert\nabla\varphi_{ion}\rVert^2\kappa^{eff}_{ion} & \text{(membrane)} \\ 0 & \text{(other zones)} \end{cases}$	W/m^3

(with an active area bigger than 100 cm^2) is quite limited. Shimpalee et al. considered the water phase change and constructed the full commercial-size 3D PEMFC model (active area 300 cm^2) [29]. However, the flow field plate design in their work was selected from US patent literature, which is different from the current commercial flow field plate.

It can be seen from the above simple review that to date, numerical research based on practical commercial PEMFC (with more than 100 cm^2 active area) is still relatively rare. The non-uniformity of key parameters under different current densities has also seldom been revealed and analyzed. Therefore for the analysis of physic quantities' in-plane distribution, there is still a large room for improvement.

In this study, a 3D two-fluid multiphase model is adopted to simulate the distributions of some key physical parameters inside a large-scale commercial PEMFC with an active area of more than 300 cm^2. Unlike the previous literature, the gap zone between the carbon paper and sealing material in the computational domain is considered. The present paper focuses on the key parameter (reactant concentration, temperature, local current density, and membrane water content) in-plane distribution characteristics along x and y directions. The average temperature, membrane water content, and concentration difference index under different average current densities are investigated. Furthermore, the influence of the change of coolant direction is analyzed. In the following, the detailed numerical model is elaborated in Section 2. Then in Section 3, simulation results of physical quantity distribution are displayed and analyzed. Finally, some conclusions are drawn in Section 4.

2. Model description

2.1. Computational domain

The PEMFC in the present study has an active area of 323 cm^2 (in Fig. 1(b)). The length and width of the membrane are shown in Fig. 1(a). A schematic diagram about the width-direction dimensions is shown in Fig. 1(b). As shown in the figure, the widths of different layers in the computational domain are not aligned. It can be observed that the widths of the bipolar plate (δ_{BP}), carbon paper ($\delta_{GDL,\ MPL}$), catalyst layer (δ_{CL}), and membrane (δ_{MEM}) are designed in the following order: $\delta_{BP}>\delta_{GDL}=\delta_{MPL}>\delta_{CL}=\delta_{MEM}$. The same is true for the length (along axis y) dimension ($l_{BP} > l_{GDL} = l_{MPL} > l_{CL} = l_{MEM}$). This design is adopted in a commercial PEMFC stack manufactured by the Dongfang Electric (Chengdu) Hydrogen Fuel Cell Technology Co., Ltd., Chengdu, China. It is different from the conventional computational domain in most published papers shown in Fig. 1(c), where the dimensions among different layers are aligned. Zone (i) in Fig. 1(b) represents the gap between carbon paper and the sealing material. Zone (ii) represents the width difference between carbon paper and the catalyst-coated membrane ($\delta_{GDL} = \delta_{MPL}>\delta_{CL}$). Besides, for the solid zone of BP, it has the biggest size in the x-y plane (in-plane area). Unless otherwise specified, the results of the present study are all based on the structure with the gap.

The serpentine channel and parallel channel are adopted in the anode and cathode flow field plates, respectively (shown in Fig. 2). It should be mentioned that due to the small flow rate in the anode side, the serpentine channel is adopted in the anode to produce enough pressure drop and remove the liquid water in anode side. The gas flow rate in the cathode is higher than the anode, which leads to a higher pressure drop and can remove the liquid water in the parallel flow field successfully. As shown in the figure, the whole flow field can be divided into the distribution zone and the mainstream zone. Both anode and cathode consist of 63 straight channels, numbered from No.1 to No.63 from the outlet side to the inlet side. One monitoring surface for presenting numerical results is selected for each channel, as shown in Fig. 2 by the red points.

2.2. Model assumptions and governing equations

2.2.1. Model assumptions

(1) The fuel cell runs under a steady condition, and all physical variables do not change with time [30,31];
(2) The flow is laminar; Both the gas species and the gas mixture follow the ideal gas law [32,33];
(3) The amount of liquid water in channels is fixed as zero, assuming that the high gas velocity in the channel could blow out the liquid water completely [34];
(4) The contact resistances between different layers are ignored [35, 36].

It should be noted that the assumption (3) is based on the

Table 2
Model parameters and empirical equations.

Parameters	Correlation	Unit
Gas mixture dynamic viscosity (x_i and φ represent the gas species mole fraction and auxiliary variable)	$\mu_g = \sum_i \frac{x_i \mu_i}{\sum_j x_j \varphi_{ij}}$ *i,j*: H_2/O_2/Vapor/N_2	Pa·s
Gas diffusivity	$D_i^{eff} = \varepsilon^{1.5}(1-s)^{1.5}\left(\frac{1}{D_i}+\frac{1}{D_{Kn}}\right)^{-1}$ *i,j*: H_2/O_2/Vapor	m^2/s
Knudsen diffusivity (r_p represents the pore diameter)	$D_{Kn} = \frac{r_p}{3}\sqrt{\frac{8RT}{\pi M_i}}$	m^2/s
Molecular diffusivity of hydrogen in the anode	$D^a_{H_2} = 1.055\times10^{-4}\left(\frac{T}{333.15}\right)^{1.5}\left(\frac{101325}{p}\right)$	m^2/s
Molecular diffusivity of oxygen in the cathode	$D^c_{O_2} = 2.652\times10^{-4}\left(\frac{T}{333.15}\right)^{1.5}\left(\frac{101325}{p}\right)$	m^2/s
Molecular diffusivity of vapor in the anode	$D^a_{vp} = 1.055\times10^{-4}\left(\frac{T}{333.15}\right)^{1.5}\left(\frac{101325}{p}\right)$	m^2/s
Molecular diffusivity of vapor in the cathode	$D^c_{vp} = 2.982\times10^{-5}\left(\frac{T}{333.15}\right)^{1.5}\left(\frac{101325}{p}\right)$	m^2/s
Capillary diffusivity of liquid water (p_c represents the capillary pressure)	$D_{lq} = -\frac{K_{lq}}{\mu_{lq}}\frac{dp_c}{ds_{lq}}$	m^2/s
Capillary pressure calculated by the Leverett-J function (σ, θ, K_0 represent the surface tension coefficient, contact angle, and intrinsic permeabilities)	$p_c = \begin{cases} \sigma\cos\theta\left(\frac{\varepsilon}{K_0}\right)^{0.5}\times[1.42(1-s_{lq})-2.12(1-s_{lq})^2+1.26(1-s_{lq})^3] & \theta<90^\circ \\ \sigma\cos\theta\left(\frac{\varepsilon}{K_0}\right)^{0.5}\times[1.42s_{lq}-2.12s_{lq}^2+1.26s_{lq}^3] & \theta>90^\circ \end{cases}$	Pa
Membrane water diffusivity (*EW* represents the Equivalent weight of MEM)	$D^{eff}_{mw} = \frac{\rho_{MEM}}{EW}4.1\times10^{-10}\left(\frac{\lambda}{25}\right)^{0.15}\left(1+\tanh\left(\frac{\lambda-2.5}{1.4}\right)\right)$	m^2/s
Saturation pressure	$\log_{10}\left(\frac{p_{sat}}{101325}\right) = -2.1749+0.02953(T-273.15)-9.1837\times10^{-5}(T-273.15)^2+1.4454\times10^{-7}(T-273.15)^3$	Pa
The phase change rate of membrane water (X_{ACL}, X_{CCL} represent the depth of anode and catalyst layer)	$\gamma' = \begin{cases} \frac{1.14\times10^{-5}}{X_{ACL}}\frac{1.8\times10^{-5}\lambda_{mw}}{5.5\times10^{-4}+1.8\times10^{-5}\lambda_{mw}}e^{2416(\frac{1}{303.15}-\frac{1}{T})} \\ \frac{4.59\times10^{-5}}{X_{CCL}}\frac{1.8\times10^{-5}\lambda_{mw}}{5.5\times10^{-4}+1.8\times10^{-5}\lambda_{mw}}e^{2416(\frac{1}{303.15}-\frac{1}{T})} \end{cases}$	1/s
Equilibrium membrane water content	$\lambda = \lambda_{eq} = \begin{cases} 0.0043+17.81a_w-39.85a_w^2+36a_w^3, 0<a_w\le1 \\ 14+1.4(a_w-1), 1<a_w\le3 \end{cases}$	
Water activity	$a_w = \frac{c_{vapor}RT}{p_{sat}}$	
Transfer coefficient	$\alpha_a = 0.25$; $\alpha_c = 0.25$	
Volumetric reference exchange current density	$j^{ref}_{0,a} = 12\times10^9$; $j^{ref}_{0,c} = 758.94$	A/m^3
Reference concentration of hydrogen; oxygen	$c^{ref}_{H_2} = 40$; $c^{ref}_{O_2} = 40$	mol/m^3

Table 3
Size and parameters of different layers.

Parameters	Value	Unit
Thickness of GDL; MPL; ACL; MEM; CCL	130; 45; 6;15; 18	μm
Width of bipolar plate (δ_{BP}); commercial carbon paper (δ_{GDL}, δ_{MPL}); catalyst layer (δ_{CL}); membrane (δ_{MEM})	11.47; 11.2; 10.8; 10.8	cm
Length of bipolar plate (l_{BP}); commercial carbon paper (l_{GDL}, l_{MPL}); catalyst layer (l_{CL}); membrane (l_{MEM})	30.57; 30.3; 29.9; 29.9	cm
Density of MEM (ρ_{MEM})	2150	kg/m^3
Equivalent weight of MEM (*EW*)	1000	kg/mol
Porosities of GDL (ε_{GDL}); MPL (ε_{MPL}); CL (ε_{CL})	0.84; 0.4; 0.3814	
Contact angles of GDL (θ_{GDL}); MPL (θ_{MPL}); CL (θ_{CL})	159; 166; 140	°
Intrinsic permeabilities of GDL (K_{GDL}); MPL (K_{MPL}); CL (K_{CL})	1.4×10^{-11}(TP)/8.5×10^{-12} (IP); 7.0×10^{-13} (TP)/1.5×10^{-12} (IP); 6.2×10^{-13}	m^2
Electrical conductivities of GDL (κ_{GDL}); MPL (κ_{MPL}); CL (κ_{CL}); BP (κ_{BP})	375(TP)/18000(IP); 90(TP)/19500(IP); 1250; 83000	S/m
Thermal conductivities of GDL ($k_{sl,GDL}$); MPL ($k_{sl,MPL}$); CL ($k_{sl,CL}$); MEM ($k_{sl,MEM}$); BP ($k_{sl,BP}$)	0.585; 0.27; 0.27; 0.109; 129	W/(m·K)
Specific heat capacities of GDL ($c_{p,GDL}$); MPL ($c_{p,MPL}$); CL ($c_{p,CL}$); MEM ($c_{p,MEM}$); BP ($c_{p,BP}$)	861; 800; 240; 1287; 710	J/(kg·K)

Table 4
Boundary and operating conditions.

Current density(A/cm^2)	0.3	0.5	0.8	1.2	1.5	1.8
A/C stoichiometry ratio	1.5/2.0	1.5/2.0	1.5/2.0	1.5/2.0	1.5/2.0	1.5/2.0
A/C back pressure (kPa)	0/0	0/0	0/0	50/50	50/50	50/50
Inlet/outlet temperature of the gas(°C)	25/50	25/50	25/50	25/50	25/50	25/50
Relative humidity	0/60%	0/60%	0/60%	0/60%	0/60%	0/58.1%
Inlet/outlet temperature of coolant(°C)	58.5/59.5	58.5/60.7	59.5/62.8	58.3/63.8	58.7/65.8	64.7/71.0

consideration that liquid water is blown away by the fast-flowing gases as soon as it immerges at the GDL/channel interface, which has been widely adopted in Refs. [34,35,37–39]. Mathematically, it can be regarded as a Dirichlet boundary condition that specifies the value of an unknown variable on the boundary.

2.2.2. Governing equations

The present study adopts a 3D two-fluid transport model to simulate the behavior of liquid, gas, electrons, and protons. The problem is governed by 12 conservation equations, including the conservation of

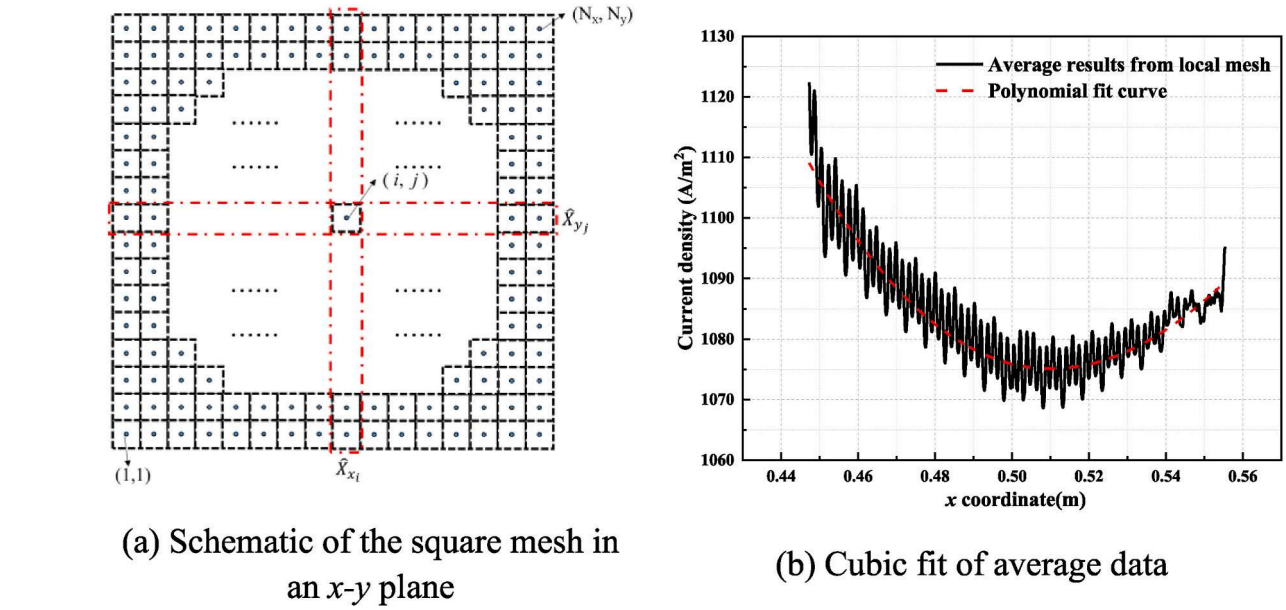

Fig. 3. Data processing method.

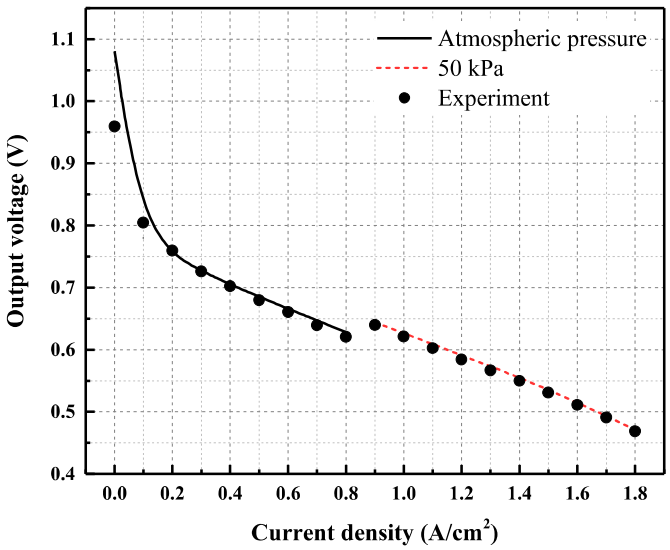

Fig. 4. Model validation.

mass, momentum, species, energy, electron/proton charge, liquid water, and dissolved water (membrane water). They are described as follows:

Mass conservation equation (solved in channels, GDLs, MPLs, CLs):

$$\nabla\cdot\left(\rho_{\mathrm{g}}\vec{u}_{\mathrm{g}}\right)=S_{\mathrm{m}} \tag{1}$$

Momentum conservation equation (solved in channels, GDLs, MPLs, CLs):

$$\nabla\cdot\left(\frac{\rho_{\mathrm{g}}\vec{u}_{\mathrm{g}}\cdot\vec{u}_{\mathrm{g}}}{\varepsilon^2\left(1-s_{\mathrm{lq}}\right)^2}\right)=-\nabla p_{\mathrm{g}}+\mu_{\mathrm{g}}\nabla\cdot\left(\nabla\left(\frac{\vec{u}_{\mathrm{g}}}{\varepsilon\left(1-s_{\mathrm{lq}}\right)}\right)+\nabla\left(\frac{\vec{u}_{\mathrm{g}}^{\mathrm{T}}}{\varepsilon\left(1-s_{\mathrm{lq}}\right)}\right)\right)-\frac{2}{3}\mu_{\mathrm{g}}\nabla\left(\nabla\cdot\left(\frac{\vec{u}_{\mathrm{g}}}{\varepsilon\left(1-s_{\mathrm{lq}}\right)}\right)\right)+S_{\mathrm{u}} \tag{2}$$

Species conservation equation of *i*-species (solved in channels, GDLs, MPLs, CLs): (*i*: H_2, O_2, water vapor)

$$\nabla\cdot\left(\rho_{\mathrm{g}}\vec{u}_{\mathrm{g}}Y_{\mathrm{i}}\right)=\nabla\cdot\left(\rho_{\mathrm{g}}D_{\mathrm{i}}^{\mathrm{eff}}\nabla Y_{\mathrm{i}}\right)+S_{\mathrm{i}} \tag{3}$$

Electrons conservation equation (solved in BPs, GDLs, MPLs, CLs):

$$0=\nabla\cdot\left(\kappa_{\mathrm{ele}}^{\mathrm{eff}}\nabla\varphi_{\mathrm{ele}}\right)+S_{\mathrm{ele}} \tag{4}$$

Protons conservation equation (solved in MEM, CLs):

$$0=\nabla\cdot\left(\kappa_{\mathrm{ion}}^{\mathrm{eff}}\nabla\varphi_{\mathrm{ion}}\right)+S_{\mathrm{ion}} \tag{5}$$

Liquid saturation conservation equation (solved in GDLs, MPLs, CLs):

$$\nabla\cdot\left(\rho_{\mathrm{l}}\frac{\mu_{\mathrm{g}}}{\mu_{\mathrm{l}}}\frac{K_{\mathrm{l}}}{K_{\mathrm{g}}}u_{\mathrm{g}}\right)=\nabla\cdot\left(\rho_{\mathrm{l}}D_{\mathrm{lq}}\nabla s_{lq}\right)+S_{\mathrm{slq}} \tag{6}$$

Dissolved water conservation equation (solved in MEM, CLs):

$$0=\frac{\rho_{\mathrm{MEM}}}{EW}\nabla\cdot\left(D_{\mathrm{mw}}^{\mathrm{eff}}\nabla\lambda_{\mathrm{mw}}\right)+S_{\mathrm{mw}} \tag{7}$$

Energy conservation equation (solved in the whole domain):

$$\nabla\cdot\left(\left(\rho c_{\mathrm{p}}\vec{u}\right)_{\mathrm{fl}}^{\mathrm{eff}}T\right)=\nabla\cdot\left(k_{\mathrm{fl,solid}}^{\mathrm{eff}}\nabla T\right)+S_{\mathrm{E}} \tag{8}$$

where ρ_g, $\vec{u}_{\mathrm{g}}$, Y_i, φ_{ele}, φ_{ion}, s_{lq}, λ_{mw}, T in Eqs. (1)–(8) denote the gas density, gas mixture velocity vector, mass fraction of species *i*, electronic potential, proton potential, liquid saturation, membrane water content, and temperature, respectively. In the momentum conservation equation, the porosity ε and permeability K (in source term) are two important parameters characterizing porous electrodes. The effective gas diffusion coefficient $D_{\mathrm{i}}^{\mathrm{eff}}$ (in Eq. (3)), electronic conductivity $\kappa_{\mathrm{ele}}^{\mathrm{eff}}$ (in Eq. (4)), and proton conductivity $\kappa_{\mathrm{ion}}^{\mathrm{eff}}$ (in Eq. (5)) take into consideration of porosity and liquid water. And the effective thermal conductivity $k_{\mathrm{fl,solid}}^{\mathrm{eff}}$ (in Eq. (8)) considers both the fluid and solid thermal conductivity. Liquid water is driven by capillary force in porous electrode, then combined with Darcy's law, the gas mixture/liquid water dynamic viscosity $\mu_{\mathrm{g}}/\mu_{\mathrm{l}}$ and capillary diffusivity of liquid water D_{lq} are imported into the liquid saturation conservation equation. The source terms in the above equations are listed in Table 1. The related key parameters are given in Table 2 and Table 3.

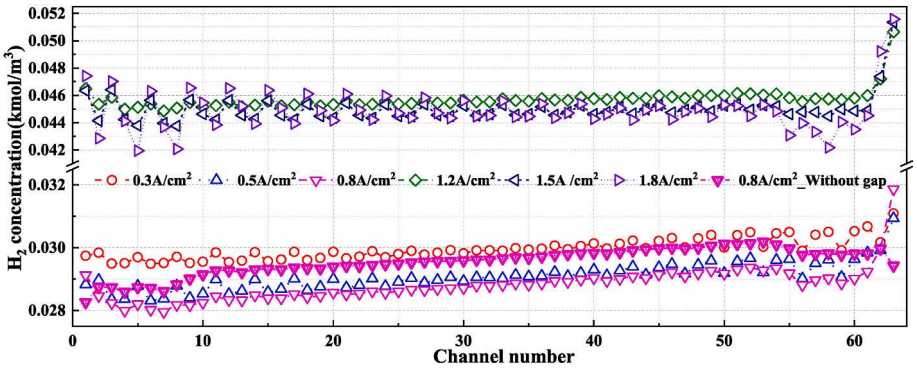

(a) H_2 concentration in anode channel

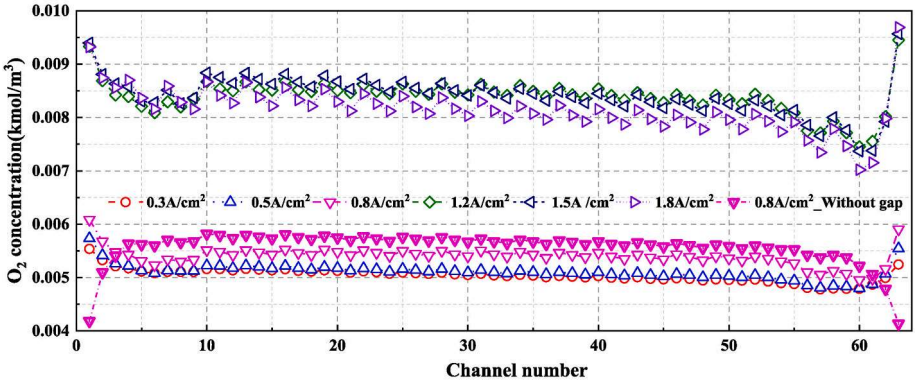

(b) O_2 concentration in cathode channel

Fig. 5. Reactant concentration in the flow channel.

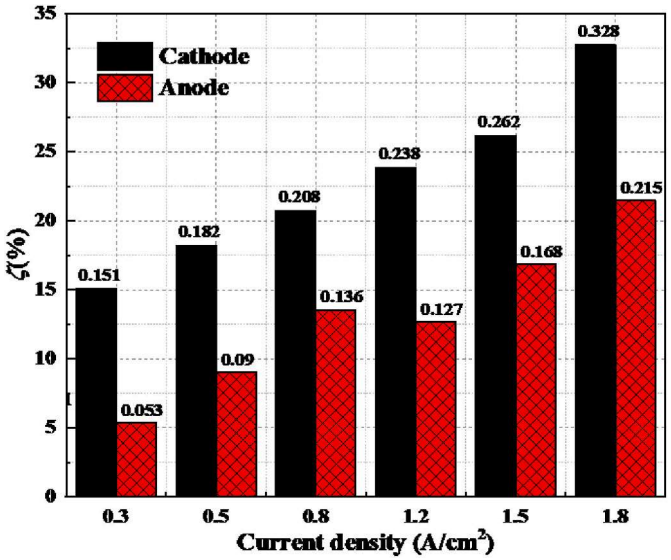

Fig. 6. The concentration difference index.

2.3. Boundary conditions and operating parameters

The boundary conditions are presented in Table 4.

For the fuel and air inlet, the mass fluxes (kg/(m^2·s)) of gas mixtures are defined respectively as

$$m_{flux,a} = \frac{\rho_a I \xi_a A_{act}}{2F c_{\text{inlet},H_2} A_{a,in}} \tag{9}$$

$$m_{flux,c} = \frac{\rho_c I \xi_c A_{act}}{4F c_{\text{inlet},O_2} A_{c,in}} \tag{10}$$

The molar concentrations of reactants are calculated by the inlet pressure $p_{a,in}$/ $p_{c,in}$, temperature $T_{a,in}$/ $T_{c,in}$, and relative humidity RH_a/ RH_c as follows:

$$c_{inlet,H_2} = \frac{p_{a,in} - RH_a p_{sat}}{RT_{a,in}} \tag{11}$$

$$c_{inlet,O_2} = \frac{0.21\left(p_{c,in} - RH_c p_{sat}\right)}{RT_{c,in}} \tag{12}$$

The relative humidity, inlet temperature, and stoichiometry ratio that appeared in Equations (9)–(12) are given for different current densities in Table 4.

The electronic potentials at the end of the anode and cathode BP

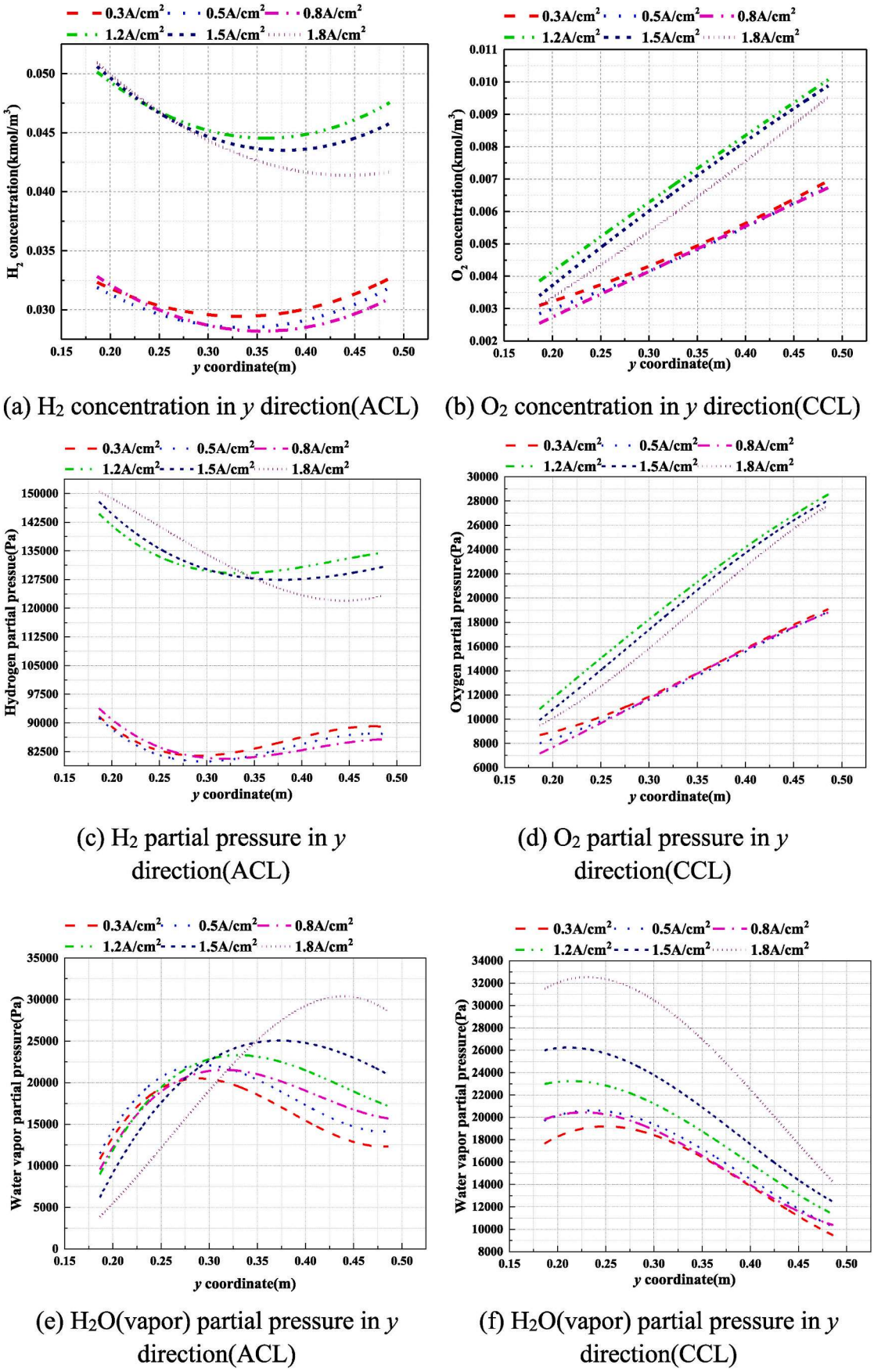

(a) H_2 concentration in y direction(ACL)

(b) O_2 concentration in y direction(CCL)

(c) H_2 partial pressure in y direction(ACL)

(d) O_2 partial pressure in y direction(CCL)

(e) H_2O(vapor) partial pressure in y direction(ACL)

(f) H_2O(vapor) partial pressure in y direction(CCL)

Fig. 7. H_2, O_2, and vapor distributions in the middle ACL/CCL.

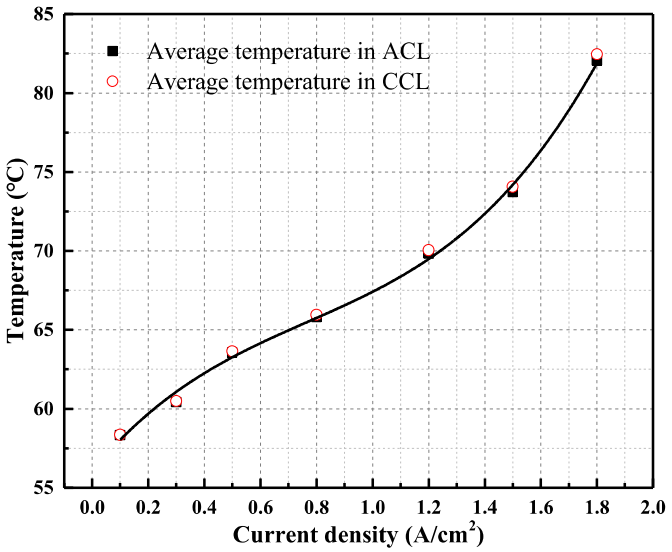

Fig. 8. Average temperature in ACL/CCL under different current densities.

surface are defined, respectively, as

$$\varphi_{ele,a} = 0 \tag{13}$$

$$\varphi_{ele,c} = E_{rev} - V_{out} \tag{14}$$

where V_{out} is the output voltage, E_{rev} is the reversible voltage which can be calculated as

$$E_{rev} = 1.229 - 0.846 \times 10^{-3}(T - 298.15) + \frac{RT}{2F}\left(\ln\frac{p_{in,H_2}}{p_0} + \frac{1}{2}\ln\frac{p_{in,O_2}}{p_0}\right) \tag{15}$$

In order to simulate the effect of coolant, the convection thermal boundary condition is specified at the anode and cathode end surface [31]. The temperature of the coolant is assumed to increase linearly from inlet to outlet, and the heat convection coefficients (HCCs) are set to be 2144 W/(m^2·K) and 2924 W/(m^2·K) in anode and cathode, respectively. These two values of HCCS are estimated from heat transfer correlation according to the dimension of the single channel (2.2 mm width and 0.4 mm depth), coolant flow rate (5.3×10^{-4} kg/s for a single cell), and heat transfer areas in the anode and cathode BP. For the details of the estimation process, see the supplementary material. The inlet and outlet coolant temperatures are given in Table 4.

The interfaces between different layers (e.g., the interface between GDL and MPL in anode or cathode) are set as interior faces. The different layers own different physical properties, which leads to different source terms or transport properties in governing equations. In Section 2.2.2, the solution zones of different governing equations are indicated in the bracket followed the title of the equation. Only the energy governing equation is solved in the whole solution domain.

2.4. Numerical procedure and grid independence test

All the governing equations stated above are solved by the software ANSYS FLUENT. The user-defined functions (UDF) written by C code are implemented to update and customize source terms, transport properties, and boundary conditions during the solving process. The grid-independent analysis is carried out on a typical unit that only contains a single channel. Then, the validated mesh size is used to construct the grid of the entire flow field. In the through-plane direction, the GDL/MPL/CL/MEM are divided into 10/7/7/8 layers, respectively. In the in-plane direction, the mesh in the distribution zone is relatively denser than in the mainstream zone. Finally, the whole computing domain is discretized into 48.15 million grids. Considering the complexity of the flow field structure in the large-scale PEMFC, it is necessary to use a small relaxation factor in the initial stage of the iterative solution. As the iteration progresses, the relaxation factor is gradually increased.

2.5. Data processing method

To better capture the in-plane distribution character of the key parameters, the simulation results are further processed to obtain the change characteristics in x (the direction from No.1 channel to No.63 channel) and y (the reaction flow direction) directions. All the meshes in the computational domain are regular hexahedral, and the square meshes in x-y plane (in-plane) are schematically shown in Fig. 3(a). The physical quantity $\widehat{X}$ can be regarded as a discrete function of the spatial position x and y, $\widehat{X} = f(x,y)$. Then the average value of the parameter $\widehat{X}$ corresponding to position x_i or position y_i could be calculated respectively by

$$\widehat{X}_{x_i} = \frac{\sum_{j=1}^{N_y} f(x_i, y_j)}{N_y}, \quad i = 1 \sim N_x \tag{16}$$

$$\widehat{X}_{y_j} = \frac{\sum_{i=1}^{N_x} f(x_i, y_j)}{N_x} \quad j = 1 \sim N_y \tag{17}$$

where N_x and N_y represent the total mesh number in x and y direction, respectively. Take current density in 0.1 A/cm^2, for example; as shown

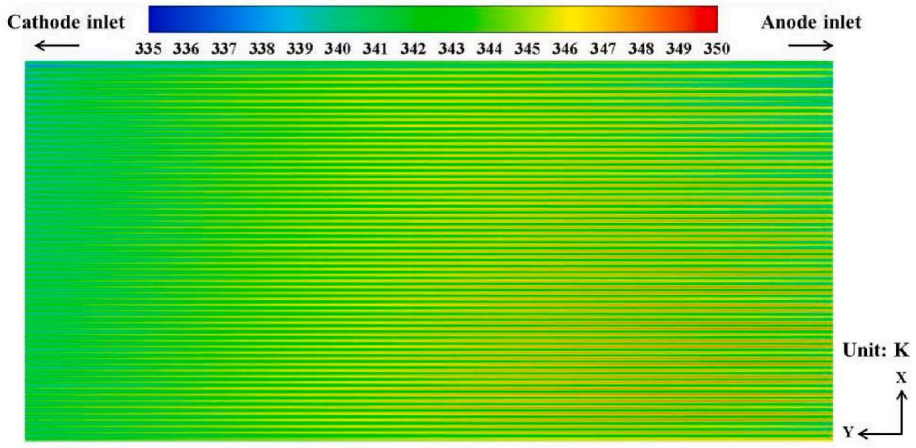

Fig. 9. Contour of temperature at 1.2 A/cm^2 in the middle plane of MEM.

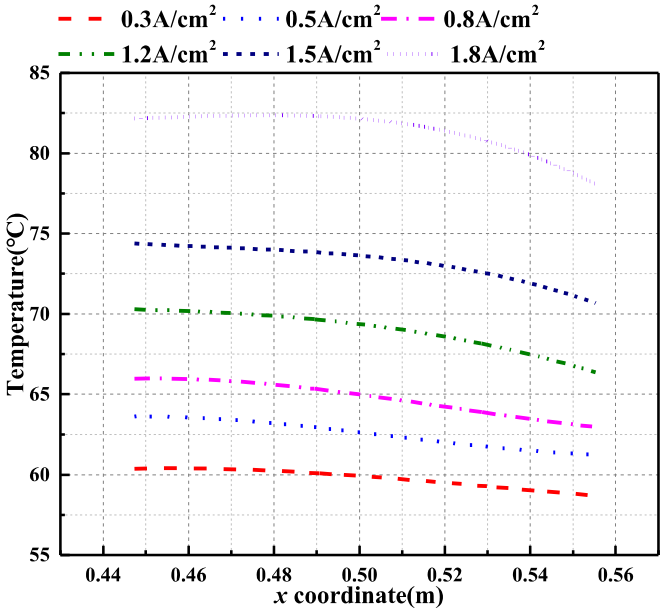

(a) Temperature in x direction

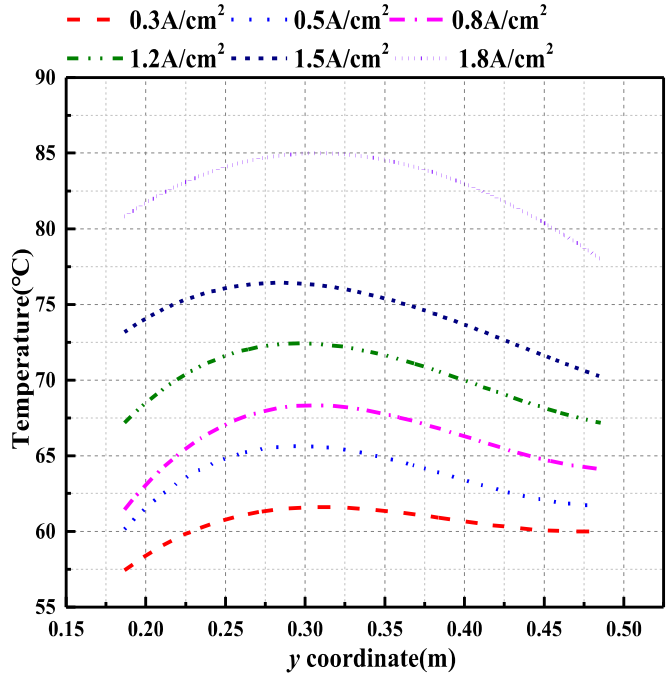

(b) Temperature in y direction

Fig. 10. Temperature distribution in the middle plane of MEM.

in Fig. 3(b), the black curve represents the change of the local current density with x position. The fluctuation of data is caused by the channel-rib structure of the flow field plate. The current density under the rib is higher than that under the channel. To reflect its essential variation character concisely, the polynomial fitting is used to smooth the data, and the red curve represents such a global variation trend. The results in the 3rd part of this paper are based on this method. The reactant concentration data are taken from the middle plane of ACL/CCL, while the temperature, current density, and membrane water data are taken from the middle plane of MEM.

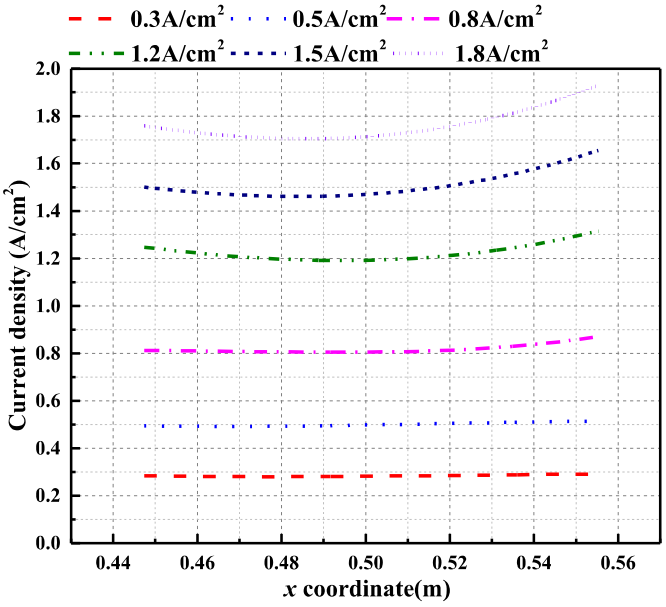

(a) Local current density distribution in x direction

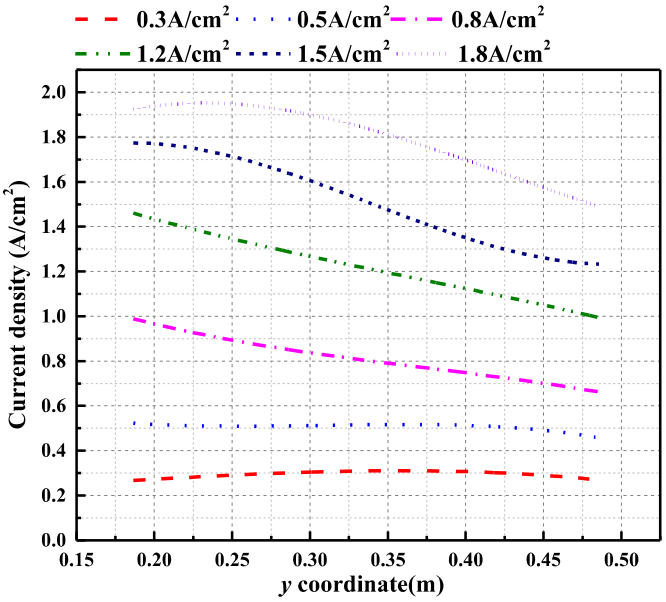

(b) Local current density distribution in y direction

Fig. 11. Local current density distribution in the middle plane of MEM.

3. Results and discussion

3.1. Model validation

The simulated polarization curve is compared with the data tested in the Long Life Fuel Cell Key Laboratory of Sichuan Province, Chengdu, China. The test conditions are listed in Table 4. The comparison results under two operating conditions are shown in Fig. 4. To increase reactant concentration under high current density, the operating gage pressure lifts from 0 (atmospheric pressure) to 50 kPa at the current density about 0.9 A/cm^2. Under the two operating conditions, the predicted polarization curve is in good agreement with the test data.

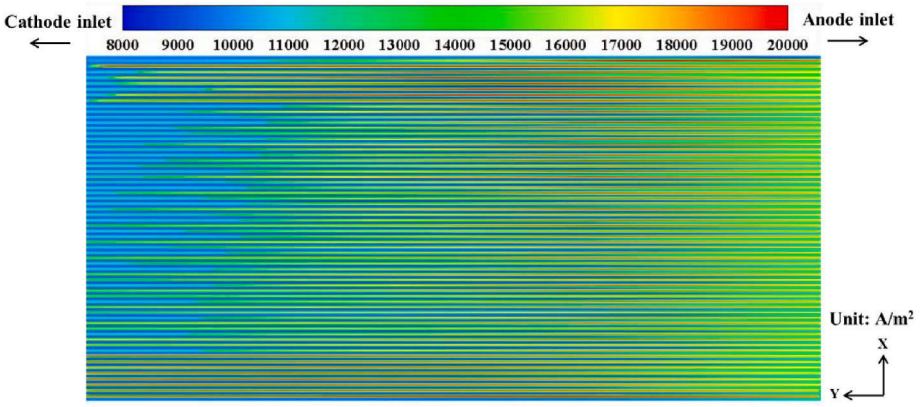

Fig. 12. Contour of local current density at 1.2 A/cm^2 in the middle plane of MEM.

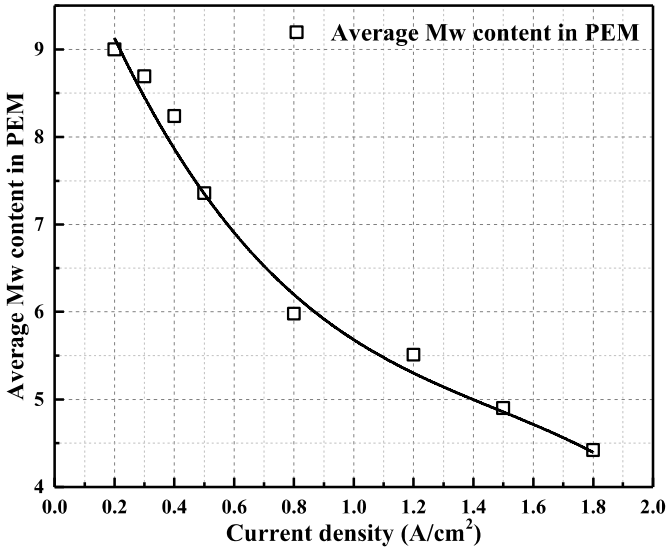

Fig. 13. Average membrane water content in PEM under different average current densities.

3.2. *Effect of average current density*

Based on the validated model, the distribution characteristics of some key physical quantities (reactant concentration, temperature, local current density, and membrane water) under different average current densities are investigated. Each physical quantity is analyzed from the *x*-direction and *y*-direction aspects, respectively. Unless otherwise stated, the resulting curves in the following passage are obtained by the method described in Section 2.5.

3.2.1. *Distribution of reactant concentration*

(1) *x*-direction

The reactant concentration values in the locations of 63 channels along the monitor surfaces of the anode and cathode shown in Fig. 2 are calculated, and the average hydrogen/oxygen concentrations are respectively shown in Figs. 5(a) and (b). The curves are divided into two groups according to different back pressures. The back pressure 0 kPa corresponds to low current density (0.3/0.5/0.8A/cm^2) and 50 kPa corresponds to high current density (1.2/1.5/1.8A/cm^2).

It can be found that both the anode and cathode have a relatively uniform distribution in the middle region. However, the concentration values in the two flow plates are quite higher at the channel edges, especially for the oxygen case. This could be explained by the existence of a gap zone (zone (i) in Fig. 1(b)). Because this zone is empty, the resistance of gas flow in this zone is relatively small. The inlet high-pressure gas flows into this zone and then is beneficial to increasing the concentration in the edge channel. In addition, there is no catalytic layer corresponding to these two regions, which will also cause the accumulation of reactants here.

For comparison, the simulation results (0.8 A/cm^2) without designing the gap zone (see the computing domain shown in Fig. 1(c)) are also plotted here. If the gap area is treated as a membrane electrode, the output voltage increase by about 1.0% (0.628 V–0.634 V), which is mainly caused by the reactant concentration. Compared with the computing domain in Fig. 1(b), there exists a bigger active area (under the same 0.8 A/cm^2 average current density). Then, the inlet mass flow rate increases, which causes a bigger pressure drop and also a bigger absolute pressure. As a result, for most channels in the middle region, the reactant concentration increases a little compared with the case with the gap. On the other hand, the reactant concentration near the edge channel decreases, especially for the cathode channel. This is due to the expansion of the catalyst layer, and the reactant near the edge channel could be consumed more quickly. Totally speaking, under the same other conditions, the performance of a cell without gaps is a little better than that with gaps. However, the latter may provide some convenience in preparation and manufacturing.

In order to quantitatively describe the non-uniformity of distribution in each channel, a concentration difference index is defined by the following formula and plotted in Fig. 6.

$$\zeta = \frac{C^{\max} - C^{\min}}{\overline{C}} \times 100\% \tag{18}$$

where $\overline{C}$ denotes the average concentration of 63 channels.

From Fig. 6, some conclusions could be drawn. First, under the same current density (0.3–1.8 A/cm^2), the concentration difference index in the cathode is higher than that in the anode. In other words, the focus of improving the flow field is on the cathode side. Second, for both the anode and cathode, the concentration difference index increases with the current density, and for the cathode, it rises to 32.8% at 1.8 A/cm^2.

According to simulation results, the concentration distribution character in the *x* direction in CL is the same as that in the channel mentioned above.

(2) *y*-direction

Figs. 7(a) and (b) present H_2 and O_2 concentration distributions along *y* direction at 6 current densities, respectively. It can be found that the oxygen concentration in the *y* direction is monotonously increasing, while the hydrogen concentration in the anode decreases firstly and then increases till to the outlet. This is also observed by the researchers in

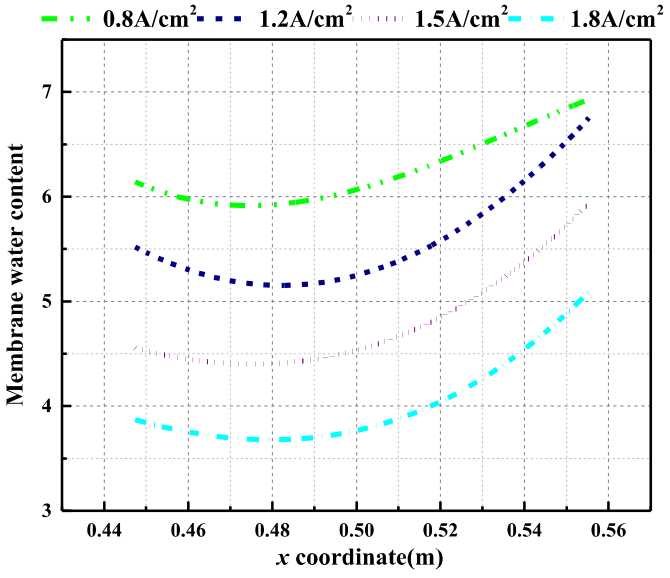

(a) Membrane water content in x direction

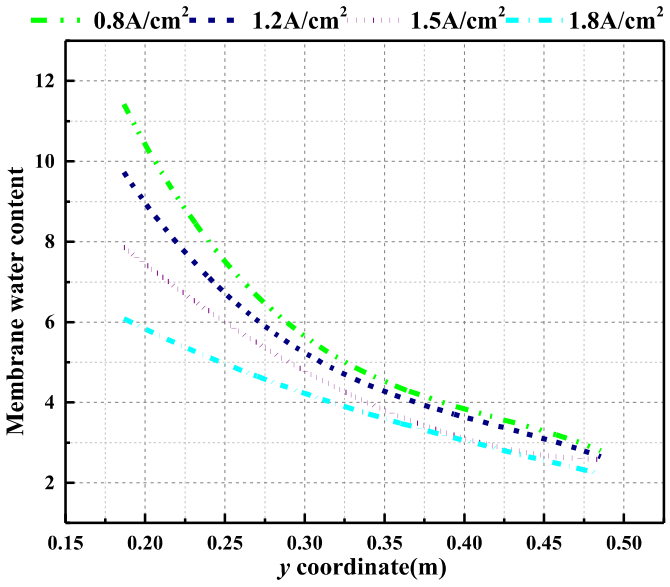

(b) Membrane water content in y direction

Fig. 14. Membrane water distribution in the middle plane of MEM.

Refs. [13,25]. Figs. 7(c) and (d) show the distribution of gas partial pressure ($p = cRT$), which is basically consistent with the gas concentration.

For the anode, the sum of the hydrogen partial pressure and the water vapor is equal to the reaction gas pressure. And as the anode inlet relative humidity is zero, the water vapor in the anode comes from the conversion of membrane water. Both hydrogen consumption in an anode reaction and an increase of water vapor content will lead to a decrease of hydrogen partial pressure. Fig. 7(e) shows the water vapor pressure variation along the y direction. Comparing Figs. 7(c) and (e), it can be found that the hydrogen and water vapor change in opposite directions. The water content at the outlet decreases, resulting in the increase of hydrogen partial pressure. Similarly, for the cathode, the oxygen partial pressure decreases as the water vapor partial pressure increases from inlet to outlet, as shown in Figs. 7(d) and (f). The effect of reaction consumption and water vapor variation is also suitable for the cathode.

3.2.2. Temperature

Fig. 8 shows the variation of average temperature in ACL/CCL with current density. It can be observed that the temperature in CCL is slightly higher than it in ACL, and the average temperature increases nonlinearly with the current density. In the range of current density less than 0.8 A/cm^2, the temperature curve concaves downward, while in the range of 0.8–1.8 A/cm^2, it concaves upward. The average temperature of the catalytic layer rises with the current density sharply. This is due to the fact that with the increase of average current density, the entropic heat of reactions, irreversible heat of the electrochemical reactions, and Joule's heat of the ohmic resistances all increase. The PEMFC should operate within a suitable temperature range. Exorbitant temperature or excess heat not only will raise the thermal load of the thermal management system, but also may deteriorate cell performance as revealed by Yan et al. [40]. They found that fuel cell performance was improved (about 51% at 0.5A/cm^2) with increasing temperature from 65 to 75 °C, unchanged between 75 and 80 °C, and begins to decrease at 85 °C. According to their study, the working temperature of the fuel cell in this study is still in a reasonable range.

About the in-plane temperature distribution, Fig. 9 shows the temperature contour in the mainstream zone at 1.2 A/cm^2. There are two low temperature zones near the gas inlet, which are caused by the low inlet gas temperature. In addition, in x direction the temperature changes up-and-down alternatively, showing the fact that the temperature under the rib is lower than that in the flow channel because the reaction heat can be quickly exported through the rib.

The temperature distributions in x and y directions in the middle plane of MEM under different current densities are shown in Fig. 10. With the increase of current density, the temperature monotonically increases. Furthermore, comparing Figs. 10(a) and (b), it is found that the temperature uniformity in the x direction is better than that in the y direction. The temperature in the x direction gradually decreases from the anode outlet side to the anode inlet side ($+x$ direction), while in the y direction it first increases and then decreases. Such variation trends are all caused by the low temperature of the inlet gas.

3.2.3. Local current density

The distribution characteristics of the local current density in x and y directions are shown in Figs. 11(a) and (b), respectively. From the figure, it can be found that the non-uniformity increases with the increase of the average current density, especially when it's over 0.5 A/cm^2. In the y direction, the current density at the cathode downstream is higher than that of the upstream. In the cathode flow field, the humidified air flows from the $+y$ side to the $-y$ side. As a result, the upstream corresponds to the position near the inlet. The downstream corresponds to the position near the outlet. In the x direction, the current density near the edge is higher than that in the middle. It will be indicated later that this distribution strongly depends on membrane water.

Fig. 12 provides the current density (at 1.2 A/cm^2) contour in the middle plane of MEM. The current density under the rib is higher than that under the channel. That is because within the present variation range, the PEMFC is working in the region of the ohmic polarization rather than concentration polarization. In other words, the effect of ohmic resistances is pronounced rather than the effect of mass transfer [41]. The ohmic resistances in the channel area are much higher than in the land area, which can be attributed to two aspects. Firstly, in relatively dry conditions, there is more membrane water content under the rib than under the channel due to a longer transport distance under the rib [42]. Secondly, the generated electrical current under the rib can be quickly derived through the solid rib, while the transport distance is longer under the channel.

3.2.4. Membrane water

The water content in the cell is crucial to the PEMFC operation, and

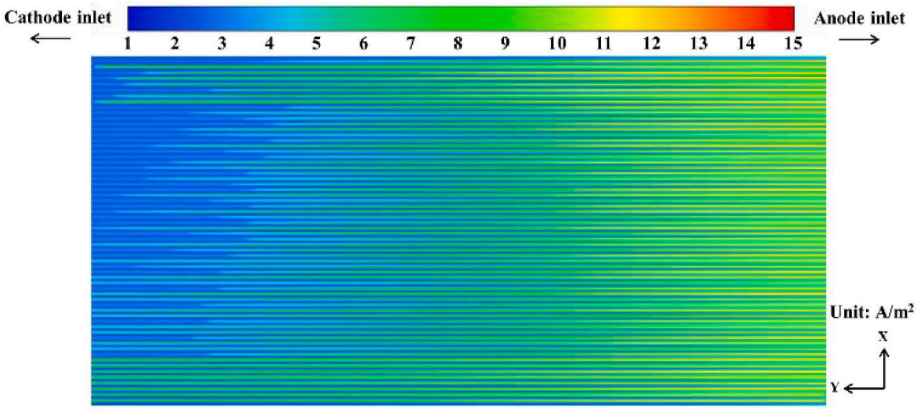

Fig. 15. Contour of membrane water content at 1.2 A/cm^2 in the middle plane of MEM.

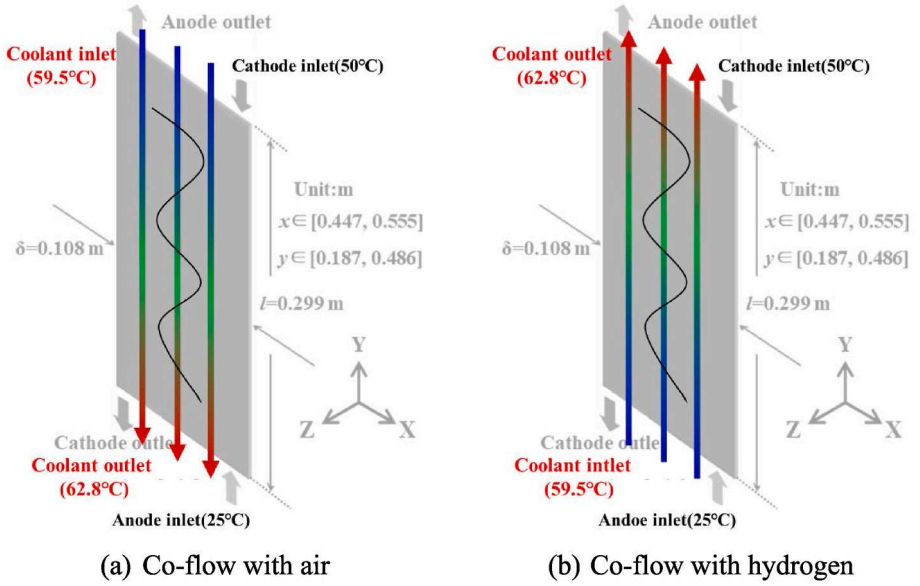

Fig. 16. Flow direction of coolant.

the membrane water content is a key parameter determining proton transport. As shown in Fig. 13, the average membrane water content decreases with the average current density, caused by the increase of temperature under the operating condition in the present study. From this, it can be inspected that the ohmic resistance (internal resistance of membrane) would increase with the average current density.

Fig. 14 (a), (b) present the membrane water content in x and y directions at the four average current densities, and Fig. 15 gives its contour at 1.2 A/cm^2. With the increase of current density, it can be observed that the temperature curve in both x and y directions in Fig. 10 moves upward, while the membrane water curve in Fig. 14 moves downward. This is consistent with the effect of temperature on membrane water content. Membrane water is produced by oxygen reduction reaction in the cathode. Then according to the local temperature and water activity, the conversion between vapor and liquid water may occur. Therefore, for the local distribution of membrane water, it is not only related to temperature but also to the direction of gas flow and the rate of the oxygen reduction reaction. In x direction, when the gas flows to the outlet side (area with a smaller x coordinate), it carries more water vapor. As a result, it promotes the formation of more membrane water, even though the temperature is higher in this region. Generally, the current density near the edge is higher than that in the middle, as shown in Fig. 14(a). In y direction, the membrane water content is lower in the cathode inlet side (area with a bigger y coordinate), even though the temperature is lower in this region. This could be explained by the lower reaction intensity, as it can be seen in the current density distribution in Fig. 11(b). Besides, from Figs. 14(b) and Fig. 15, it can be found that the membrane water content at the cathode downstream is higher than that at the upstream. This is related to the water vapor flow direction in the cathode. Comparing Figs. 12 and 15, it can be observed that the distribution of membrane water is similar to that of the current density. They are coupled with each other. On the one hand, the amount of membrane water content is determined by the reaction intensity. On the other hand, the local membrane water content has an effect on the local reaction or the generation of electrical current.

3.3. *Effect of coolant flow direction*

In this section, the effect of coolant flow direction, either co-flow with hydrogen or co-flow with air, is investigated under the same output voltage. The output voltage V_{out} = 0.628 V (@ 0.8 A/cm^2) remains unchanged, and the cooling water flow direction is changed; that is, the thermal boundary is modified as shown in Fig. 16. Figs. 17(a) and (b) show the temperature distribution along the x and y direction, respectively. As can be seen in Fig. 17(a), the temperature difference in the x direction between the two flow directions is very small (no more

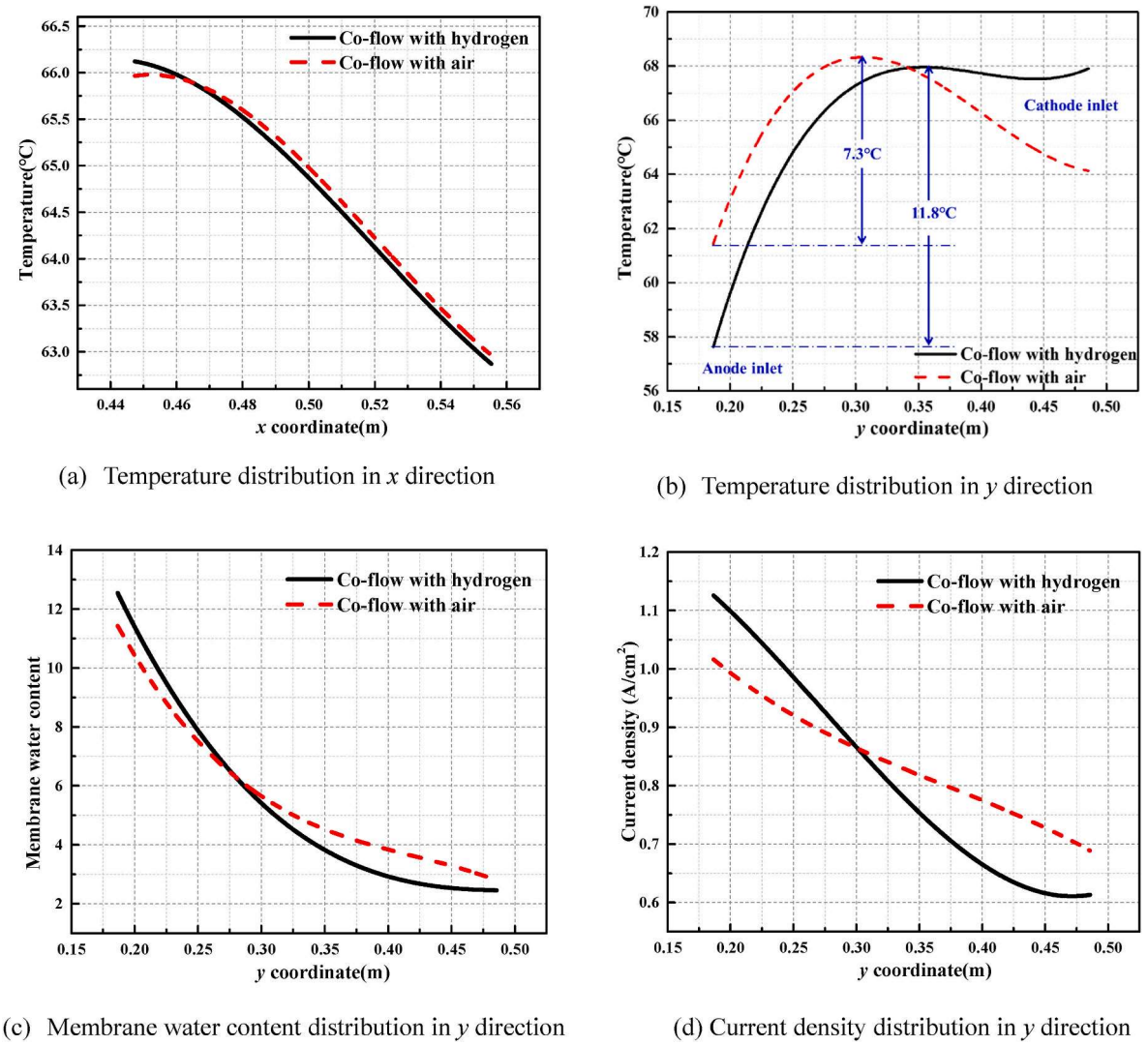

Fig. 17. Effect of the coolant flow direction on the temperature, membrane water, and current density distribution in the middle plane of MEM.

than 0.2 °C). In addition, between the two coolant flow directions, the other physical quantities also change little in the *x* direction.

For the *y* direction, the two temperature distribution curves intersect at about mid-point, and exhibit the difference in temperature uniformity. The inlet temperature of humidified air and hydrogen is 50 °C and 25 °C, respectively. The temperature of the coolant rises from 59.5 °C at the inlet to 62.8 °C at the outlet. When the coolant co-flow with the hydrogen, the hotter coolant appears on the hotter air inlet side (area with a bigger y coordinate), while the cooler coolant appears on the cooler hydrogen inlet side (area with a smaller y coordinate). This reduces the temperature difference of convective heat transfer, which is not conducive to heat dissipation. As a result, compared with the co-flow with the air, the temperature near the anode inlet is lower, and vice versa near the cathode inlet. As shown in Fig. 17(b), the temperature range of co-flow with air and hydrogen is 7.3 °C and 11.8 °C, respectively. This temperature variation pattern causes correspondingly variation in membrane water content, as shown in Fig. 17(c). That is the higher the temperature, the lower the membrane water content. Furthermore, the dehydrated membrane reduces the chemical reaction rate, resulting in a low current density, as shown in Fig. 17(d). Although the local current density increases somewhere and decreases somewhere, finally, as a whole, the average current density decreases. It is found that for the co-flow with hydrogen, the average current density decreases from 0.8 A/cm^2 to 0.77 A/cm^2 (3.75% decrease) compared the co-flow with air under the same output voltage.

4. Conclusions

In the present study, a 3D two-fluid transport model is established to study the distribution characteristics of some key parameters in a commercial-size PEMFC with an active surface area of 323 cm^2. The main findings of this study are as follows.

(1) Two PEMFC structures (with or without gap zone) result in different reactant concentrations by affecting the inlet mass flow rate. In the structure without gap zone, the reactant concentration in most channels increases, and the cell performance increases about 1%.
(2) The in-plane distribution uniformity of key physical quantities is as follows: the non-uniformity of cathode reactant distribution is generally higher than that of the anode; The non-uniformity of temperature in the *x* direction is higher than that in the *y* direction (flow direction); The non-uniformity of local current density increases with the increase of average current density; The distribution of membrane water is similar to the current density.
(3) The temperature rises faster and faster when the cell is working under a high average current density, and it will lead to

membrane dehydration. This demonstrates the importance of water and thermal management.

(4) When the cell works under the ohmic polarization region, the current density under the rib is higher than that under the channel. While the temperature under the rib is lower than that under the channel, due to that the heat could be quickly exported from the solid rib.

(5) When the flow direction of coolant changes from co-flow with the air to co-flow with the hydrogen, the local value of membrane water and current density will change. And as a whole, it cause the total average current density decrease 3.75%.

Author statement

Zhuo Zhang: Conceptualization, Methodology, Software, Writing - Original Draft, **Qiyao Wang:** Resources, Validation, **Fan Bai:** Software, **Li Chen:** Project administration, Wen-**quan Tao:** Writing- Reviewing and Editing, Supervision.

Declaration of competing interest

The authors declare that they have no known competing financial interests or personal relationships that could have appeared to influence the work reported in this paper.

Data availability

Data will be made available on request.

Acknowledgments

The study is supported by the projects of the National Key Research & Developement Program (2018yfb1502504-02), NNSFC (51836005, 51911530157), The Basic research Project of Shaanxi Province (Grant number 2019ZDXM3-01) and the Key Science and Technology Projects in Sichuan Province (2019ZDZX0002).

Appendix A. Supplementary data

Supplementary data to this article can be found online at https://doi.org/10.1016/j.energy.2022.125897.

References

[1] Branco CM, El-kharouf A, Du S. Materials for polymer electrolyte membrane fuel cells (PEMFCs): electrolyte membrane, gas diffusion layers and bipolar plates. In: Olabi A-G, editor. Encyclopedia of smart materials. Oxford: Elsevier; 2022. p. 378–88.

[2] Zhang Z, He P, Dai Y-J, Jin P-H, Tao W-Q. Study of the mechanical behavior of paper-type GDL in PEMFC based on microstructure morphology. Int J Hydrogen Energy 2020;45:29379–94.

[3] Wang Y, Ruiz Diaz DF, Chen KS, Wang Z, Adroher XC. Materials, technological status, and fundamentals of PEM fuel cells - a review. Mater Today 2020;32:178–203.

[4] Jiao K, Xuan J, Du Q, Bao Z, Xie B, Wang B, Zhao Y, Fan L, Wang H, Hou Z, Huo S, Brandon NP, Yin Y, Guiver MD. Designing the next generation of proton-exchange membrane fuel cells. Nature 2021;595:361–9.

[5] Fan L, Tu Z, Chan SH. Recent development of hydrogen and fuel cell technologies: a review. Energy Rep 2021;7:8421–46.

[6] Peng L, Shao H, Qiu D, Yi P, Lai X. Investigation of the non-uniform distribution of current density in commercial-size proton exchange membrane fuel cells. J Power Sources 2020;453:227836.

[7] Moçotéguy P, Ludwig B, Beretta D, Pedersen T. Study of the impact of reactants utilization on the performance of PEMFC commercial stacks by impedance spectroscopy. Int J Hydrogen Energy 2021;46:7475–88.

[8] Chen Y-S, Peng H, Hussey DS, Jacobson DL, Tran DT, Abdel-Baset T, Biernacki M. Water distribution measurement for a PEMFC through neutron radiography. J Power Sources 2007;170:376–86.

[9] Xiao B, Zhao J, Tu Z, Chan SH. Water distribution and performance variation in a transparent PEMFC with large active area. Int J Hydrogen Energy 2021;46:38040–50.

[10] Chevalier S, Ge N, George MG, Lee J, Banerjee R, Liu H, Shrestha P, Muirhead D, Hinebaugh J, Tabuchi Y, Kotaka T, Bazylak A. Synchrotron X-ray radiography as a highly precise and accurate method for measuring the spatial distribution of liquid water in operating polymer electrolyte membrane fuel cells. J Electrochem Soc 2016;164:F107–14.

[11] Suzuki T, Tabuchi Y, Tsushima S, Hirai S. Measurement of water content distribution in catalyst coated membranes under water permeation conditions by magnetic resonance imaging. Int J Hydrogen Energy 2011;36:5479–86.

[12] Cheng Z, Luo L, Huang B, Jian Q. Effect of humidification on distribution and uniformity of reactants and water content in PEMFC. Int J Hydrogen Energy 2021;46:26560–74.

[13] Yin C, Gao Y, Li T, Xie G, Li K, Tang H. Study of internal multi-parameter distributions of proton exchange membrane fuel cell with segmented cell device and coupled three-dimensional model. Renew Energy 2020;147:650–62.

[14] Belhadj M, Aquino A, Heng J, Kmiotek S, Raël S, Bonnet C, Lapicque F. Current density distributions in polymer electrolyte fuel cells: a tool for characterisation of gas distribution in the cell and its state of health. Chem Eng Sci 2018;185:18–25.

[15] Huang B, Jian Q, Luo L, Bai X. Research on the in-plane temperature distribution in a PEMFC stack integrated with flat-plate heat pipe under different startup strategies and inclination angles. Appl Therm Eng 2020;179:115741.

[16] Akimoto Y, Okajima K, Uchiyama Y. Evaluation of current distribution in a pemfc using a magnetic sensor probe. Energy Proc 2015;75:2015–20.

[17] Lin R, Zhu Y, Ni M, Jiang Z, Lou D, Han L, Zhong D. Consistency analysis of polymer electrolyte membrane fuel cell stack during cold start. Appl Energy 2019;241:420–32.

[18] Ma Y, Lin R, Hou Z, Wang R, Wang Y, Ji W. Research on the variation of current density distribution in a commercial-size proton exchange membrane fuel cell under dynamic gas operation parameters. Int J Heat Mass Tran 2022:196.

[19] Zhong D, Lin R, Jiang Z, Zhu Y, Liu D, Cai X, Chen L. Low temperature durability and consistency analysis of proton exchange membrane fuel cell stack based on comprehensive characterizations. Applied Energy; 2020. p. 264.

[20] Tang Y-Q, Fang W-Z, Lin H, Tao W-Q. Thin film thermocouple fabrication and its application for real-time temperature measurement inside PEMFC. Int J Heat Mass Tran 2019;141:1152–8.

[21] Zhang G, Wu J, Wang Y, Yin Y, Jiao K. Investigation of current density spatial distribution in PEM fuel cells using a comprehensively validated multi-phase non-isothermal model. Int J Heat Mass Tran 2020;150:119294.

[22] Hao L, Moriyama K, Gu W, Wang C-Y. Three dimensional computations and experimental comparisons for a large-scale proton exchange membrane fuel cell. J Electrochem Soc 2016;163:F744–51.

[23] Xie B, Ni M, Zhang G, Sheng X, Tang H, Xu Y, Zhai G, Jiao K. Validation methodology for PEM fuel cell three-dimensional simulation. Int J Heat Mass Tran 2022;189:122705.

[24] Falagüerra T, Muñoz P, Correa G. Analysis of the cathode side of a PEMFC varying design parameters to optimize current distribution and power density. J Electroanal Chem 2021;880:114820.

[25] Chen H, Liu B, Zhang T, Pei P. Influencing sensitivities of critical operating parameters on PEMFC output performance and gas distribution quality under different electrical load conditions. Appl Energy 2019;255:113849.

[26] Cheng Z, Luo L, Huang B, Jian Q. Effect of humidification on distribution and uniformity of reactants and water content in PEMFC. Int J Hydrogen Energy 2021;46:26560–74.

[27] Zhang G, Xie X, Xie B, Du Q, Jiao K. Large-scale multi-phase simulation of proton exchange membrane fuel cell. Int J Heat Mass Tran 2019;130:555–63.

[28] Liu H, Zhang G, Li D, Wang C, Bai S, Li G, Wang G. Three-dimensional multi-phase simulation of cooling patterns for proton exchange membrane fuel cell based on a modified Bruggeman equation. Appl Therm Eng 2020;174:115313.

[29] Shimpalee S, Hirano S, DeBolt M, Lilavivat V, Weidner JW, Khunatorn Y. Macro-scale Analysis of large scale PEM fuel cell flow-fields for automotive applications. J Electrochem Soc 2017;164:E3073–80.

[30] Jiao K, He P, Du Q, Yin Y. Three-dimensional multiphase modeling of alkaline anion exchange membrane fuel cell. Int J Hydrogen Energy 2014;39:5981–95.

[31] Chen X, Yu Z, Yang C, Chen Y, Jin C, Ding Y, Li W, Wan Z. Performance investigation on a novel 3D wave flow channel design for PEMFC. Int J Hydrogen Energy 2021;46:11127–39.

[32] Xiong K, Wu W, Wang S, Zhang L. Modeling, design, materials and fabrication of bipolar plates for proton exchange membrane fuel cell: a review. Appl Energy 2021;301:117443.

[33] Lin C, Yan X, Wei G, Ke C, Shen S, Zhang J. Optimization of configurations and cathode operating parameters on liquid-cooled proton exchange membrane fuel cell stacks by orthogonal method. Appl Energy 2019;253:113496.

[34] Mu Y-T, He P, Ding J, Tao W-Q. Modeling of the operation conditions on the gas purging performance of polymer electrolyte membrane fuel cells. Int J Hydrogen Energy 2017;42:11788–802.

[35] Zhang G, Jiao K. Multi-phase models for water and thermal management of proton exchange membrane fuel cell: a review. J Power Sources 2018;391:120–33.

[36] Chen H, Guo H, Ye F, Ma CF. Modification of the two-fluid model and experimental study of proton exchange membrane fuel cells with baffled flow channels. Energy Convers Manag 2019;195:972–88.

[37] Yan X, Guan C, Zhang Y, Jiang K, Wei G, Cheng X, Shen S, Zhang J. Flow field design with 3D geometry for proton exchange membrane fuel cells. Appl Therm Eng: Design, processes, equipment, economics 2019;147:1107–14.

[38] Cao T-F, Mu Y-T, Ding J, Lin H, He Y-L, Tao W-Q. Modeling the temperature distribution and performance of a PEM fuel cell with thermal contact resistance. Int J Heat Mass Tran 2015;87:544–56.

[39] Sahraoui M, Bichioui Y, Halouani K. Three-dimensional modeling of water transport in PEMFC. Int J Hydrogen Energy 2013;38:8524–31.
[40] Yan Q, Toghiani H, Causey H. Steady state and dynamic performance of proton exchange membrane fuel cells (PEMFCs) under various operating conditions and load changes. J Power Sources 2006;161:492–502.
[41] Jia S, Liu H. Direct measurement of lateral current density distribution in a PEM fuel cell with a serpentine flow field. Int J Hydrogen Energy 2014;39:1449–56.
[42] Shrivastava UN, Tajiri K, Chase M. Current density and ohmic resistance distribution in the land-channel direction of a proton exchange membrane fuel cell. J Power Sources 2015;299:189–94.